

Numerical Simulation of Flow Resistance due to the *Limnoperna fortunei*

Attachment

Qingqing Hou¹, Chengfan Sun¹, Yuncheng Xu^{1,2,3}, and Mengzhen Xu⁴

¹ College of Water Resources and Civil Engineering, China Agricultural University, Beijing, China.

² Beijing Engineering Research Center of Safety and Energy Saving Technology for Water Supply Network System, Beijing, China.

³ Engineering Resources Center of Agricultural Water-Saving and Water Resources, Ministry of Education, Beijing, China.

⁴ State Key Laboratory of Hydrosience and Engineering, Tsinghua University, Beijing, China.

Corresponding author: Y. Xu (ycxu@cau.edu.cn)

M. Xu (mzxu@mail.tsinghua.edu.cn)

Key Points:

- Generation & analysis of geometric models of adult *Limnoperna fortunei* (LF) attachments, considering mussel densities & size variations
- Development of a numerical modeling scheme to replicate the flow over the LF attachment with internal periodic boundary conditions
- LF attachments reducing local velocity & boosting turbulence, and increasing the Manning's n value in skimming flow by over 90%

Abstract

High-density attachment of *Limnoperna fortunei* (LF) would lead to the increase of flow resistance, which has posed big challenges to the normal operation of water conveyance projects. It is very necessary to quantify the flow resistance caused by the attachment of LF. In this study, a 3D geometric model of LF was generated based on real images. Attachment models of LF were generated with different densities and mussel size distributions, whose geometric characteristics were evaluated by some fundamental physical quantities, including attachment thickness, bed coverage, surface vertical roughness, and roughness concentration. Furtherly, a 3D numerical model with specific boundary conditions was established in OpenFOAM to simulate the flow over the LF attachment. Body-fitted mesh was generated using *snappyHexMesh* based on the LF attachment model. The results show that in high-density scenarios, a big wake zone formed inside LF attachment by the combined effects of each individual LF. Turbulence kinetic energy distribution indicated that LF attachment would cause viscous dissipation thus leading to more energy loss. The flow structure inside LF attachment was controlled by the mussel size and spacing between each mussel. Manning's n values were calculated based on the CFD results at different densities. The results show that the flow resistance of LF attachment also followed the classic flow regimes, where in the skimming flow regime, the mussel size distribution played a non-negligible role. Higher flow speed resulted in larger flow resistance, and n could increase more than 90% compared to the scenario without LF attachment.

1 Introduction

In recent years, inter-basin water transfer projects have increased dramatically due to human water management needs, and long-distance water transfers pose a serious risk of biological invasions (Barbosa et al., [2018](#); Pyšek et al., [2020](#); Haubrock et al., [2022](#); Zhang et al., [2022](#); Mahapatra et al., [2023](#)). These aquatic organisms have spread to many parts of the world, such as North American, South American, and European continents (de Medeiros Fortunato & Andrade Figueira, [2022](#); Elizarraga et al., [2023](#)). Their attachment corrodes concrete walls, increases flow resistance, clogs pipes and damages the structure of man-made buildings (Boltovskoy et al., [2022](#); de Souza et al., [2023](#)), which cost \$ 63.7 billion (2017 US\$) across all regions and socio-economic sectors between 1980 and 2020 (Haubrock et al., [2022](#)). China also faces a significant risk of invasion by *Limnoperna fortunei* (LF) from its warm water source in South China (Zhan

et al., [2015](#); Wang et al., [2023](#); Wang et al., [2023](#); Yang et al., [2024](#)). When LFs are in the planktotrophic larvae stage, they flow with the water which causes a rapid spread through the water transfer channel (Ricciardi, [1998](#); Nakano et al., [2012](#); Cataldo, [2015](#)). Byssal attachment occurs in a selected suitable habitat, and the dissoconch will soon become adult (Morton, [2015](#)). When the adult LF is under suitable conditions of ecological amplitude and flow speed, the attachment density increases rapidly (Xu et al., [2015](#); Zhao et al., [2019](#); Liu et al., [2020](#)), resulting in the variation of the flow resistance as well (Li, [2009](#); Yan & Sun, [2019](#)). Nevertheless, the changes in flow resistance due to LF attachment increase the unpredictability of hydraulic calculations for open channels, which posed a great potential threat to the operation of water transfer projects. Some hydrodynamic variables, such as velocity (Zhang et al., [2020](#)), wall shear stress (French & Ackerman, [2014](#)), and vortex structure (Lazzarin et al., [2023](#)) were used to describe the impact of mussel attachment on the flow field (Hardison & Layzer, [2001](#); Allen & Vaughn, [2010](#); Lopez & Vaughn, [2021](#)). However, the quantification of the flow resistance due to LF attachment structures remains unresolved.

Flow resistance controls the energy losses due to viscous dissipation (Smith, [2014](#)), thus scholars use experiments and numerical simulations to quantify flow resistance generated by the presence of roughness elements. In both natural rivers and water transfer channels, the aquatic organisms as well as other in-stream structures attached to the bottom walls can be considered as roughness elements in hydrodynamics (Styles, [2015](#); Xu & Liu, [2017](#); Yang & Nepf, [2019](#); Ismail et al., [2021](#)). The flow field around such roughness elements can be divided into three regimes (Morris, [1955](#); Mayaud et al., [2016](#); Sansom et al., [2020](#)): isolated roughness flow, wake-interference flow, and skimming flow, based on bed coverage (%) (Davis & Barmuta, [1989](#); Friedrichs et al., [2000](#)) and dimensionless physical quantity roughness concentration (Lee & Soliman, [1977](#); Sansom et al., [2022](#)), where the isolated roughness flow occurred when percent bed coverage was less than 5% or roughness concentration was less than 0.082, the wake interference occurred when percent bed coverage was 5% to 8% or roughness concentration was 0.082 to 0.198, and the skimming flow occurred when percent bed coverage was over 12% or roughness concentration was over 0.198. In previous studies, many efforts have been made to quantify the flow resistance due to the streambeds. In mountain streams, flow resistance was found to be maximized at the roughness concentration of 0.2-0.4 (Canovaro et al., [2007](#)). In vegetated channels, it was found that flow resistance was connected to the patch-scale vegetation

distribution, rather than the geometry of single plant (Nepf, [2012](#)), the drag coefficient was studied for an emergent vegetated patch area under nonuniform flow (Zhang et al., [2024](#)). In Chen et al. ([2019](#))’s study, different sizes of streambed sediment were scanned and reconstructed based on structure-from-motion (SfM) photogrammetry, and they discovered that the stream flow resistance was mainly controlled by the standard deviation of the bed elevation normalized by water depth. As for these aquatic organisms, the species, sizes, densities and distribution may play important roles in flow resistance (Ghisalberti, [2009](#); Wang et al., [2010](#); Mossa et al., [2017](#); He et al., [2021](#)). Therefore, some hydraulic models incorporate the geometric features of the roughness elements to increase the prediction of flow resistance (D’Ippolito et al., [2021](#)).

Freshwater mussels, as an important component of the aquatic system, cover an increasing area of the bottom bed in water transfer projects. Therefore, the flow resistance generated by their attachment to the wall cannot be not ignored. The presence of both live and dead mussel shells increase benthic surface area and shear stress (Vaughn & Hakenkamp, [2001](#); Zimmerman & De Szalay, [2007](#)). Early studies of ship resistance in 1916 showed that fouled plates exposed to seawater had four times the frictional resistance of new smooth plates (McEntee, [1916](#)). When the percent bed coverage of the mussels reached 100%, the overall structure and underlying substrate of the streambed or boat bottom were changed (Widdows et al., [2002](#)). Different sizes of *Barnacle* attached to the ship bottom increased the flow resistance, leading to power loss of up to 86% at cruising speed (Schultz, [2007](#)). As a further study, the effect of roughness on the frictional resistance of a ship could be well predicted with a uniform distribution of the organisms (Demirel et al., [2017](#)). Experimental studies showed that the attachment of *Mytilus edulis* (55% - 95% bed coverage) enhanced the turbulent kinetic energy and wall shear stresses (Widdows et al., [2009](#)). After further quantification of the hydraulic elements, the mussel-covered streambed increased wall shear velocity by 28% and bed roughness by nearly 300% (Sansom et al., [2018](#)). When the density of *Lampsilis siliquoidea* exceeded 25 mussels/m² on the wall surface, the turbulent shear stresses acting on the mussels were reduced by up to 64% (Sansom et al., [2020](#)). The study of the flow field structure around the mussels revealed that vortex structures were formed around the mussels, which increased the wall shear stress and induced local scour in front and behind the mussel (Lazzarin et al., [2023](#)). In most studies of mussel roughness, the studied species were much larger than LF, thus the pervious findings may

be not applicable for LF. Moreover, the non-uniform distribution of mussel size has not been considered yet.

CFD-based numerical simulations have been more and more popular for the studies of the flow field around aquatic organisms (Wu et al., [2020](#); Xu & Liu, [2021](#); Wu & Constantinescu, [2022](#)). By resolving the complex geometric structures of the aquatic organisms, forces acting on the objects as well as the local flow structures could be accurately predicted (Xu & Liu, [2017](#); Chen et al., [2018](#); Lazzarin et al., [2023](#)). Therefore, high-resolution geometric models are crucial to ensure the accuracy of numerical simulations. Turbulence modeling also plays an important role in CFD simulation of mussel attachment. Khor & Xiao ([2011](#)) used Standard $k - \varepsilon$ turbulence model to simulate the effect of biofouling, indicating that the pressure gradient increased gradually with the height of attachment. Constantinescu et al. ([2013](#)) used large eddy simulation (LES) to simulate the turbulence structures around a group of freshwater mussels, which were also validated by PIV measurements. Wu et al. ([2020](#)) used Spalart-Allmaras model (Spalart & Allmaras, [1992](#)) in their simulation, and a positive correlation was found between the current force acting on the mussel shells and the ratio of the exposed height and length of the mussel shells. Song et al. ([2020](#)) used Unsteady Reynolds Averaged Navier-Stokes (URANS) model to simulate the roughness effect of biofouling on ship bottom, and established the relationship between roughness and factors such as Froude number. Lazzarin et al. ([2023](#)) used the Detached Eddy Simulation (DES) in STAR-CCM+ to resolve flow field among the partially-buried mussels.

To quantify the flow resistance due to the attachment of non-uniform and high-density distribution of LF, the following objectives were fulfilled: 1) geometric structures of LF attachment with different densities and size distributions were generated properly; 2) geometric parameters of the LF attachment were carefully calculated and analyzed; 3) a numerical model featured with internal periodic boundary condition was proposed to simulate the flow over the LF attachment, obtaining rich information about mass transfer and momentum exchange; 4) Manning's n value was also used to quantify the overall roughness effect of LF attachment under different flow conditions.

2 Geometric models

2.1 *Limnoperna fortunei* attachment

The size of adult mussel shells usually varied in the north and south of China due to environmental factors such as water temperature (Liu et al., 2020). According to the previous sampling data in the main channel of grand water diversion project, the lengths of the adult LF shells were greater in the south than that in the north (Fu & Bin, 2012; Wei et al., 2015; Zhao et al., 2019; Yang et al., 2024). In this study, the average size of the adult LF model was determined to be 22.0 mm in length in the south and 17.0 mm in length in the north. Based on the front-view image, the anterior edge of the adult shell is nearly rounded, and it is connected to the posterior edge to form a large arc. From the view of dorsal side, the adult shells are slightly swollen and narrowed posteriorly, with the ligaments of the adult shells located in the medial side. From the ventral side, the adult shell has a narrow undercut and the shell outline is diamond-shaped. Thus, the geometric model of an individual adult LF was built in Blender as shown in Figure 1c.

Carefully considering the size of an individual adult LF, a 20 cm \times 20 cm plane was selected to place a certain density of LF, so as to mimic the attachment of LF. Due to the maximum LF shell length limitation in the south, the highest achievable density for a single-layer LF is 15000 ind/m². Any density exceeding this limit would result in multi-layer attachment. Similarly, the maximum density in the north is 20000 ind/m². To ensure the non-overlapping and randomness of attachment, the density of the attachment model used in this study was set from 500 ind/m² to 20,000 ind/m². Obviously, the actual LF attachment naturally comprises mussel shells of diverse sizes. The mussel length frequency distribution for the south and north, based on the sampling data provided by Yang et al., 2024, is illustrated in Figure 1b. Accordingly, the size of each individual LF in the attachment model was set randomly based on the length frequency. In addition, the location and orientations of each individual LF placed on the plane are randomized. The placement of LF on the plane were processed by activating the falling action of the physical motion engine in Blender, and the plane was set as stationary rigid body. The placement process for each density was replicated three times to yield three unique 20 cm \times 20 cm LF attachment planes, with the intention of capturing a certain degree of bio-attachment diversity. For convenience of discussion, the attachment model in the south is denoted as S_{am} , and the north

model is denoted as N_{am} . The LF attachment models were generated as STL (STereoLithography) file format, which is actually triangulated surface mesh. STL files can be easily used as input to generate 3D mesh in OpenFOAM.

Then, the geometric features of the LF attachment models were examined by several geometric parameters, including maximum and mean thickness, bed coverage, surface vertical roughness, and roughness concentration. These geometric parameters not only provide a quantitative description of the attachment model, but also provide a basis for further investigation of flow resistance, thus promoting the further development of roughness elements research. It should be noted that this study focused on the mechanisms of flow resistance induced by a single-layer attachment instead of multi-layer attachment.

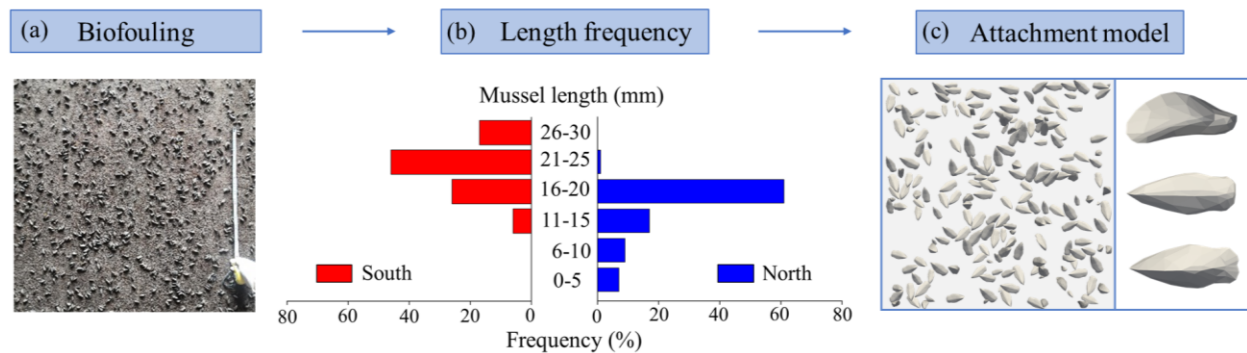


Figure 1. Geometric models of the *Limnoperna fortunei* (a) biofouling; (b) the frequency of mussel length in southern and northern China; (c) visualizations of an individual LF model and attachment model

2.2 Attachment thickness

The attachment thickness refers to the height of the roughness elements, which is a fundamental physical quantity for describing the attachment of aquatic organisms. In this study, the mean height H_0 and the maximum height H_m are used to describe the thickness of the attachment model. The maximum height refers to the vertical distance between the lowest and the highest points of the attachment model, which is easy to obtain. The mean height was calculated by averaging the height of each LF in the attachment model, which can be done using Python scripts.

In order to evaluate the randomness of the attachment model, the standard deviation of attachment thickness was calculated for each same density. The relationship between density and

attachment thickness is shown in Figure 2. It can be seen that H_m is close to the maximum length of the individual. H_0 gradually increases with the attachment density, with a significantly steeper increase in the south compared to the north, likely due to the different length distributions in the respective regions. The small and consistent deviation in attachment thickness at the same density indicates that the current random placement method is suitable for modeling attachments.

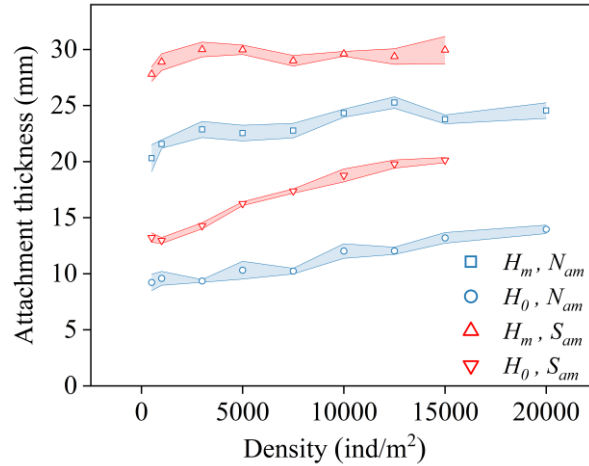


Figure 2. The thickness of LF attachment model at each density for both South (S_{am}) and North (N_{am})

2.3 Bed coverage

Bed coverage is one of the most important physical quantities for bio-attachment, which has been linked to flow resistance in many studies (Manga & Kirchner, 2000; Demirel et al., 2017; Nugroho et al., 2023). Using bed coverage to quantify the effect of mussels on the wall would be more effective than using density because different mussels vary in size, whereas bed coverage considers only the contact area and is independent of mussel size. The bed coverage is calculated as following (Sansom et al., 2022):

$$C_b = \frac{\sum A''}{A_{total}} \quad (1)$$

where C_b is the bed coverage (%) occupied by mussels on the bed; A'' is the area occupied by an individual mussel (m^2); A_{total} is the total planar area (m^2).

Figure 3 shows the C_b of LF at different distances from the wall in the south and north. Due to the randomness of the attachment position and orientation, C_b varied greatly at different

distances from the wall. It also turned out to be significantly different for different attachment densities. Overall, higher density resulted in larger C_b . For each density, C_b was greatest at the distance of 5-10 mm from the wall both south and north. When establishing the fitting relationship between roughness concentration and bed coverage, the maximum bed coverage at each density was used for the calculations.

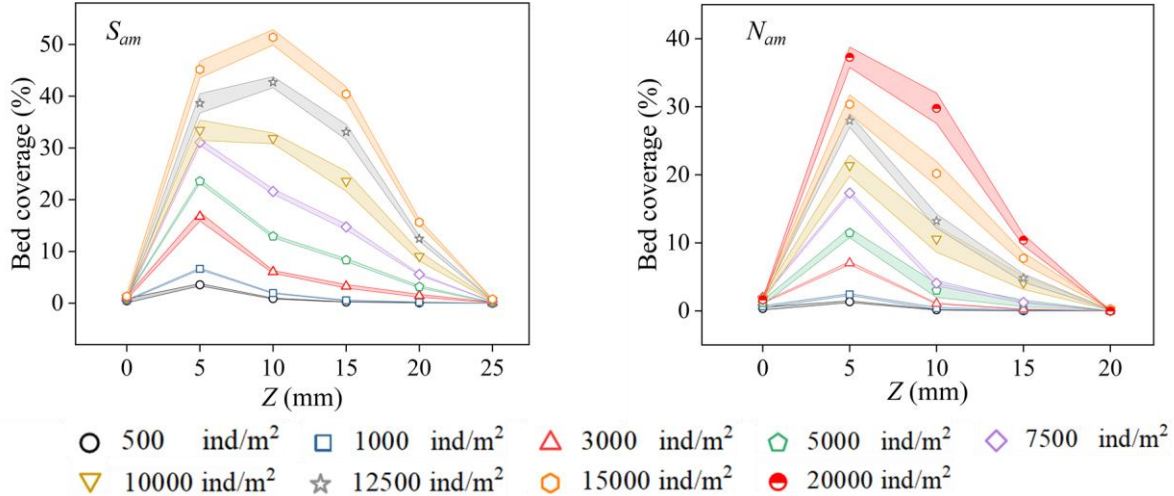


Figure 3. Bed coverage (%) of LF attachment model at the different distances from the wall (a) South (S_{am}) (b) North (N_{am})

2.4 Surface vertical roughness

The standard deviation of all the individual LF height in each attachment model can be calculated as the surface vertical roughness as follows (Nikora et al., 1998; Aberle & Smart, 2003):

$$\sigma_z = \sqrt{\frac{1}{m-1} \sum_{i=1}^m (H_i - H_0)^2} \quad (2)$$

where σ_z is surface vertical roughness (mm); m is the number of LF (ind.); H_i is the height of each individual in the attachment model (mm); H_0 is the mean height of the attachment model (mm).

Figure 4 shows the variation of σ_z at different densities. In the south, σ_z increases first, and then decreases, with a maximum value at density of 5000 ind/m², while in the north, it increases with density and then gradually stabilizes at the density of 10000 ind/m². It also indicated that the trend of σ_z variation at different densities were related to the length distribution of mussels.

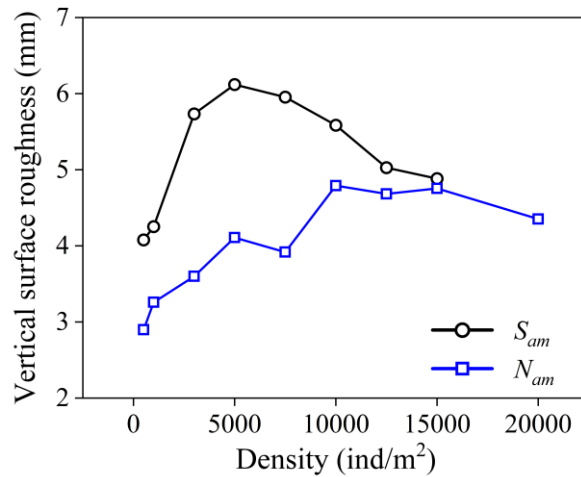


Figure 4. The surface vertical roughness of LF attachment models at each density for both south and north

2.5 Roughness concentration

In order to relate the attachment thickness of roughness element to the density, roughness concentration was calculated by multiplying the projected area by the density, as follows:

$$L_c = A'D \quad (3)$$

where L_c denotes the roughness concentration; A' denotes the projected area of the attachment model (m²/ind); D denotes the density of the attachment model (ind/m²).

In the process of calculating the projected area, researchers used to assume mussels as ellipses because of the its irregularity in shape (Wolfe & Nickling, 1993; Sansom et al., 2022). In this paper, an octree algorithm was used to calculate the exact projected area of the attachment model in order to speed up the computation.

The relationship between the bed coverage (C_b) and roughness concentration (L_c) were carefully examined. Data of different densities from both south and north were plotted in Figure 5. It turned out that these tow variables fitted well with a quadratic function. It should be noted

that the maximum C_b at each density was selected as the fitting data. Since it is difficult to directly obtain the L_c under actual attachment conditions, the bed coverage can be measured or photographed instead. The advantage of this fitting function is that it is independent of the size distribution of the mussels and is therefore applicable to a wide range of attachments.

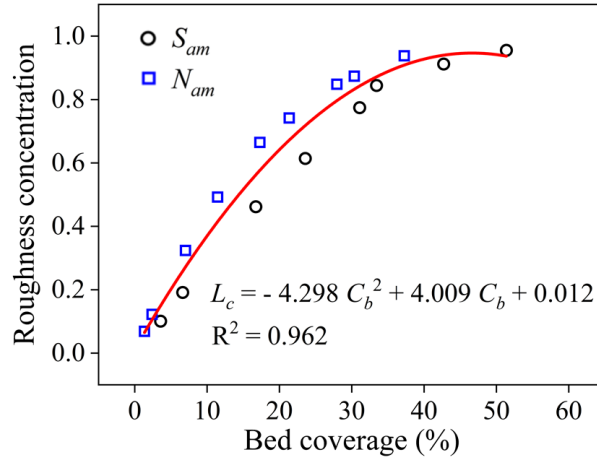


Figure 5. Relationship between bed coverage (%) and roughness concentration

3 Numerical Simulation

3.1 Governing equations

Eddy-resolving turbulence models such as LES (Constantinescu et al., 2013) and DES (Lazzarin et al., 2023) were used to simulate the flow around mussels. However, compared to the previous study, the individual mussels in this study were significantly smaller and their attachment was much denser, resulting in increased computational requirements. Therefore, *SST k - ω* RANS model was used instead in this study. The governing equations can be found as follows:

$$\frac{\partial \bar{u}_i}{\partial x_i} = 0 \quad (4)$$

$$\frac{\partial}{\partial t} \left(\frac{\bar{u}_i^2}{2} \right) + \bar{u}_j \frac{\partial}{\partial x_j} \left(\frac{\bar{u}_i^2}{2} \right) = \frac{\partial}{\partial x_j} \left(-\frac{\bar{p}}{\rho} \bar{u}_j + 2\nu \bar{s}_{ij} \bar{u}_i - \overline{u'_i u'_j \bar{u}_i} \right) - 2\nu \overline{s_{ij} s_{ji}} + \overline{u'_i u'_j s_{ij}} \quad (5)$$

250 where \bar{u}_i is the resolved velocity; $\frac{\partial}{\partial t} \left(\frac{\bar{u}_i^2}{2} \right) + \bar{u}_j \frac{\partial}{\partial x_j} \left(\frac{\bar{u}_i^2}{2} \right)$ denotes the change rate of the mean
 251 kinetic energy; $\frac{\partial}{\partial x_j} \left(-\frac{\bar{p}}{\rho} \bar{u}_j + 2\nu \bar{s}_{ij} \bar{u}_i - \overline{u'_i u'_j \bar{u}_i} \right)$ denotes the mean kinetic energy transport due to
 252 the mean pressure; $2\nu \bar{s}_{ij} \bar{s}_{ji}$ represents the mean kinetic energy transport due to the viscous stress;
 253 $\overline{u'_i u'_j \bar{s}_{ij}}$ represents the mean kinetic energy transport due to the Reynolds stress.

254 The attachment of LF to the wall acts as a barrier to water flow, thereby increasing the viscous
 255 stress on the solid wall surface and converting the average kinetic energy into internal energy,
 256 ultimately leading to flow resistance.

257 SST $k - \omega$ turbulence model combines the advantages of both the $k - \omega$ and the $k - \varepsilon$ turbulence
 258 models (Menter, [1994](#)). The governing equations of k and ω can be found as follows:

259 k equation:

$$\frac{\partial \rho k}{\partial t} + \frac{\partial (\rho \bar{u}_j k)}{\partial x_j} = P_k - D_k + \frac{\partial}{\partial x_j} \left((\mu + \sigma_k \mu_t) \frac{\partial k}{\partial x_j} \right) \quad (6)$$

261 where P_k is the turbulent kinetic energy (TKE) generation term, which reflects the relationship
 262 between the time-averaged Reynolds stress and the time-averaged velocity gradient; and D_k is
 263 the turbulent kinetic energy destruction term, which reflects the turbulent dissipation rate.

264 ω equation:

$$\frac{\partial \rho \omega}{\partial t} + \frac{\partial (\rho \bar{u}_j \omega)}{\partial x_j} = P_\omega - D_\omega + \frac{\partial}{\partial x_j} \left((\mu + \sigma_\omega \mu_t) \frac{\partial \omega}{\partial x_j} \right) + 2\rho(1 - F_1) \frac{\sigma_{\omega 2}}{\omega} \frac{\partial k}{\partial x_j} \frac{\partial \omega}{\partial x_j} \quad (7)$$

266 where P_ω is the turbulence-specific dissipation generation term, reflecting the relationship with
 267 the eddy viscosity coefficient; D_ω is the turbulence-specific dissipation law destructive term; μ
 268 is the hydrodynamic viscosity coefficient; ω is specific turbulence dissipation rate; F_1 is the
 269 mixing function term, the turbulence model is mainly through the adjustment of the value of F_1
 270 to achieve the conversion in the $k - \varepsilon$ and $k - \omega$ turbulence model.

In this study, all the numerical simulation cases were performed in OpenFOAM v8 (The OpenFOAM Foundation, 2020). *pimpleFoam* was adopted as the solver with adjustable time-step.

3.2 Boundary conditions

In real world, water flows are generally fully developed. However, in numerical simulation, it is difficult to set the inlet as the fully developed boundary condition. In this study, the inlet boundary condition (BC) of U , k , and ω was set as *mapped* in OpenFOAM, which refers to internal periodic boundary condition. The basic idea of this BC is that for each time step, the values on the inlet cross-section are mapped from the last-time-step values on a certain cross-section some distance downstream, and the mapped values are adjusted to reach a pre-set average value, which are used as Dirichlet BC for inlet in current time step. In OpenFOAM, BCs need to be set for each variable. The setup of BCs used in this study can be found in Table 1. The free surface (top) was treated as free-slip rigid lid, namely *symmetryPlane*. In order to focus on the impact of LF attachment, side-wall effects were not considered in this study. Thus, side walls in the numerical models were set as periodic boundary condition namely *cyclicAMI*. Numerically, the two side walls are connected to each other, to form an infinitely wide channel. In this case, this numerical model is more like a fully developed boundary layer flow. The computational domain and boundary conditions are shown in Figure 6a. Detailed explanations of all the BCs can be found on any official website of OpenFOAM.

According to the literature (Jing et al., 2022), Fr in the main channel was chosen between 0.09 and 0.29 in the numerical simulation. Therefore, the mean values of the incoming flow velocity (U_0) were set as 0.20 m/s, 0.25 m/s, 0.30 m/s when the water depth (H_0) was 0.5 m, and the U_0 were set as 0.20 m/s, 1.00 m/s and 2.00 m/s when H_0 was 5.0 m. Cases using hydraulically smooth wall as bottom (without LF attachment) were performed for these scenarios. Figure 6b shows the vertical distribution of the simulated streamwise velocity in dimensionless form, all of which matched well with the theoretical result for smooth walls.

Table 1 Setup of boundary condition of the variables used in OpenFOAM

	U	p	K	ω	ν
inlet	<i>mapped</i>	<i>zeroGradient</i>	<i>mapped</i>	<i>mapped</i>	<i>calculated</i>

outlet	<i>pressureInlet-OutletVelocity</i>	<i>totalPressure</i>	<i>inletOutlet</i>	<i>inletOutlet</i>	<i>calculated</i>
sideWalls	<i>cyclicAMI</i>	<i>cyclicAMI</i>	<i>cyclicAMI</i>	<i>cyclicAMI</i>	<i>cyclicAMI</i>
bottom/LF	<i>noSlip</i>	<i>zeroGradient</i>	<i>kqRWallFunction</i>	<i>omegaWallFunction</i>	<i>nutUSpalding-WallFunction</i>
top	<i>symmetryPlane</i>	<i>symmetryPlane</i>	<i>symmetryPlane</i>	<i>symmetryPlane</i>	<i>symmetryPlane</i>

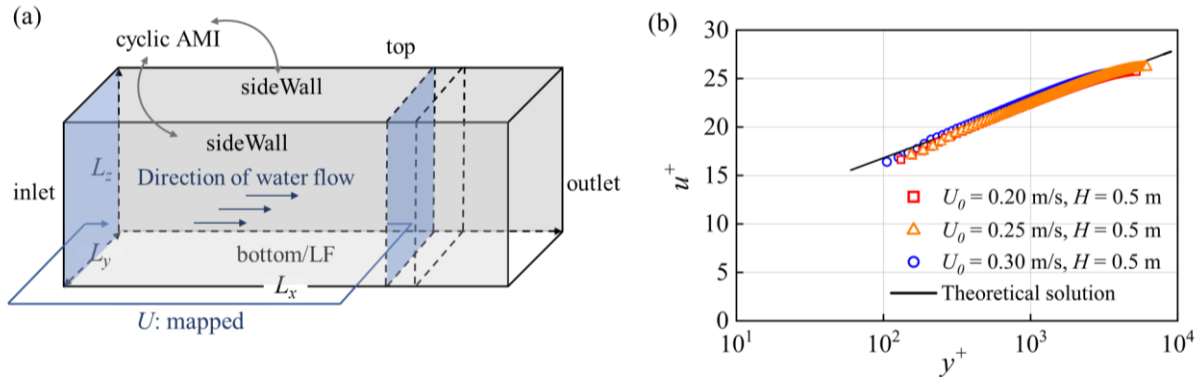


Figure 6. (a) 3D model of smooth wall and boundary conditions: L_x , L_y and L_z denote the length, width and height of the computational domain, respectively (b) vertical distribution of streamwise velocity in dimensionless form for cases with smooth walls

3.3 Mesh generation

Following the statement in section 2.1, *snappyHexMesh*, a mesh-generation tool in OpenFOAM, was utilized to generate the body-fitted mesh of the computation domain over LF attachment, based on the surface mesh of LF attachment model. As shown in Figure 7a, three randomly generated LF attachment model (200 mm in length) with same density and size distribution were placed accordingly in upstream part (600 mm in total length). In order to improve the performance of the inlet internal mapping process, 5 mm gaps were set at both the inlet cross-section and mapping cross-section (about 600 mm from the inlet). Pre-testings showed that 5 mm gap would not affect the simulation results but greatly improve the robustness of the numerical model. There was another 190 mm distance between the location of mapping cross-section and the outlet, which was testified to be long enough to eliminate the effect of outlet overflow. As shown in Figure 7b, the grid in the near-wall region was refined to improve computational efficiency. Grid independence analysis shown in Figure 7c indicated that the mesh with 1.2 million cells was good enough for the prediction of the manning roughness coefficient. In order

to facilitate the simulation, a pre-case with coarser mesh was performed firstly. Then, a case with finer mesh mapped the result from the pre-case, and used it as initial condition. The y^+ distribution is shown in Figure 7d.

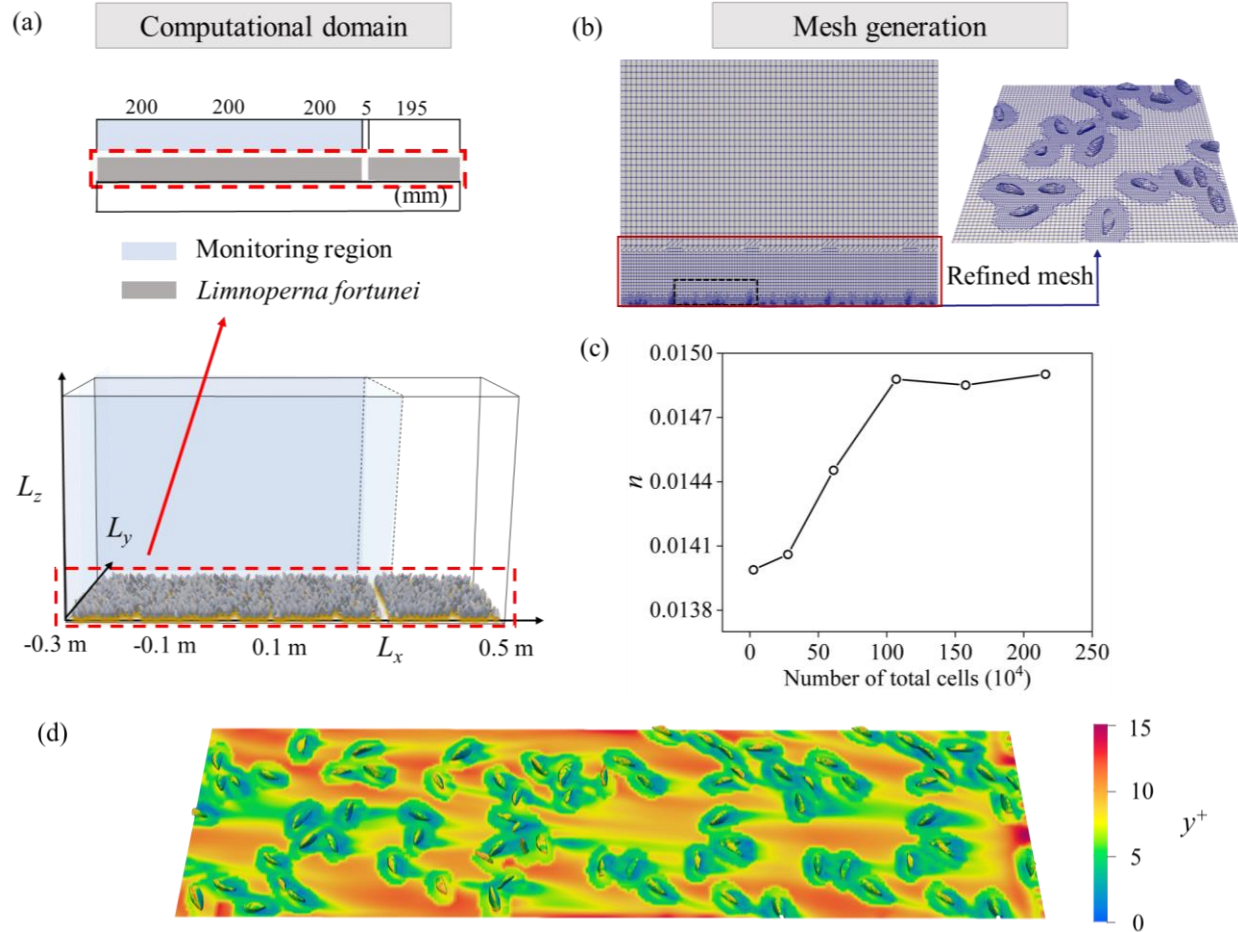


Figure 7 Mesh generation using *snappyHexMesh* (a) placement of LF attachment models on the bed (b) refined grids of the LF attachment model (c) grid independence analysis of manning roughness coefficient (d) y^+ distribution: 500 ind/m²

4 Results and discussions

4.1 Near-wall flow field

In order to minimize the possible numerical effects of inlet and outlet, the region with L_x from -0.1 m to 0.1 m was selected for further analysis. For the south LF size distribution, the mean

length of LF is $L_0 = 0.02$ m, which will be used as a non-dimensional indicator to investigate the effect of LF on both velocity and turbulence kinetic energy distribution.

Horizontal velocity distribution at certain distances from the bottom bed was shown in Figure 8, with $U_0 = 0.25$ m/s. In the streamwise velocity (u_x) distribution, the disturbance due to individual LF, such as wake zones, can be clearly identified in the low-density scenarios. In the high-density scenarios, u_x turned out to be much smaller inside the LF attachment (at distance of $0.5L_0$ from the bed), which could be regarded as a result of the combing effect of each individual LF. In the transverse velocity (u_y) distribution, the disturbance caused by LF was small compared to u_x , but still identical in the near-wall region. Especially, the combining effects of LF on u_y seemed to be independent of density inside the LF attachment. It should be noted that the effect of the LF attachment could be also found outside the LF attachment (at distances of $1.5L_0$ and $2L_0$ from the bed).

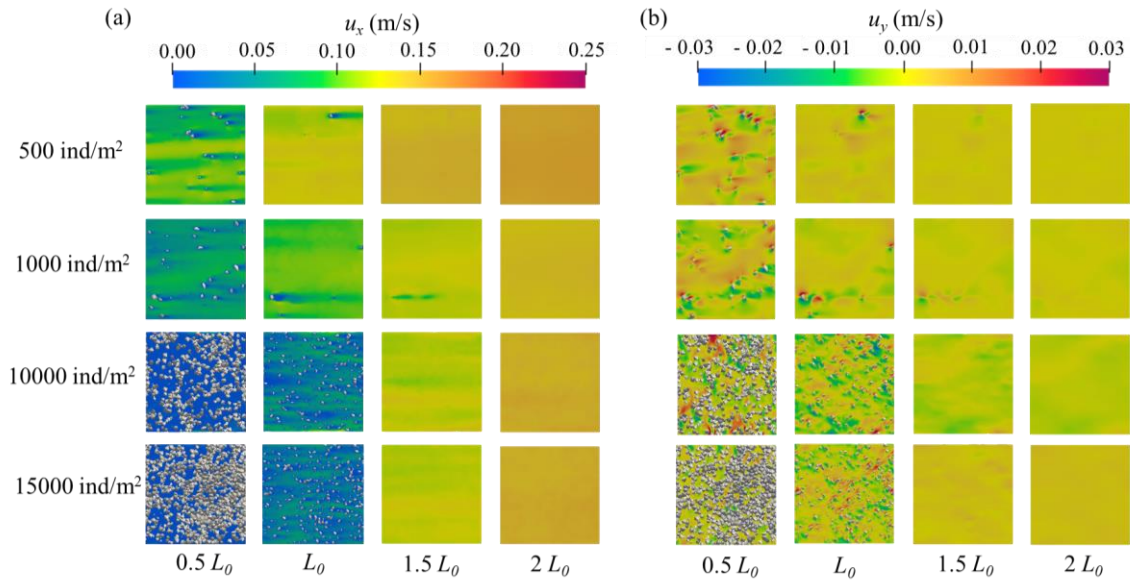


Figure 8. Velocity distribution at different distances from the bottom bed, $U_0 = 0.25$ m/s (a) streamwise velocity; (b) transverse velocity ($L_0 = 0.02$ m, which is the mean length of LF, $0.5L_0$, L_0 , $1.5L_0$, $2L_0$ denotes the distance of 0.01 m, 0.02 m, 0.03 m and 0.04 m from the bottom bed)

Turbulent kinetic energy (k) was calculated from Eq. (6), which is commonly used to denote the magnitude of turbulence intensity. Figure 9 shows k distribution at different distances from the bottom bed, with $U_0 = 0.25$ m/s. Since k is strongly related to velocity, its distribution was very similar to u_x . However, in the canopy layer of LF attachment (at distances of $0.5L_0$ and L_0 from

the bed), k tended to increase in the wake zone of individual LF, which cannot be identified inside LF attachment. Overall, low-density LF attachment tended to generate higher k . One possible reason could be that viscous dissipation occurs as a result of the flow resistance due to LF attachment.

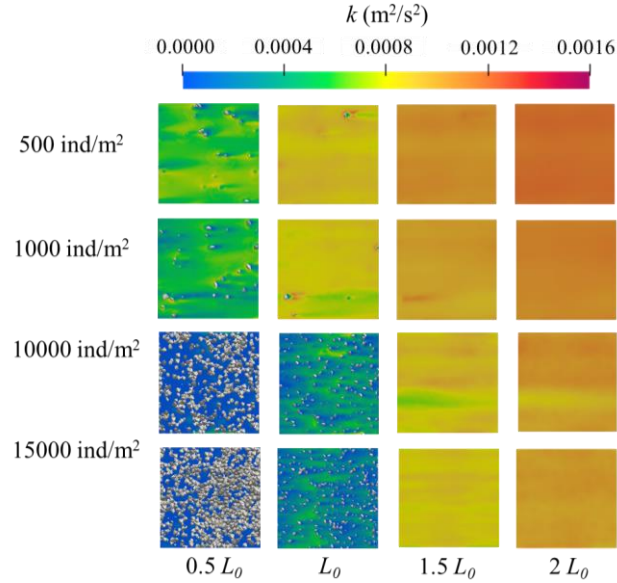


Figure 9. Turbulent kinetic energy distribution at different distances from the bottom bed, $U_0 = 0.25$ m/s ($L_0 = 0.02$ m, which is the mean length of LF, $0.5 L_0$, L_0 , $1.5 L_0$, $2 L_0$ denotes the distance of 0.01 m, 0.02 m, 0.03 m and 0.04 m from the bottom bed)

4.2 Flow structure near LF attachment

There is not specific definition on flow structure. In this study, the flow structures were visualized by λ_2 criterion in post-processing of OpenFOAM. The flow structure visualization is accomplished by contour extraction, which can fully identify the vortices in the three-dimensional velocity field (Jeong & Hussain, 1995). The flow structures for different attachment densities are shown in Figure 10, at $\lambda_2 = 1$, colored by velocity magnitude. It indicated that although richer coherent flow structures could be found in high-density scenarios, the structure size appeared to be similar at different densities. The size of the flow structures appeared to be controlled by the size and spacing between each individual LF.

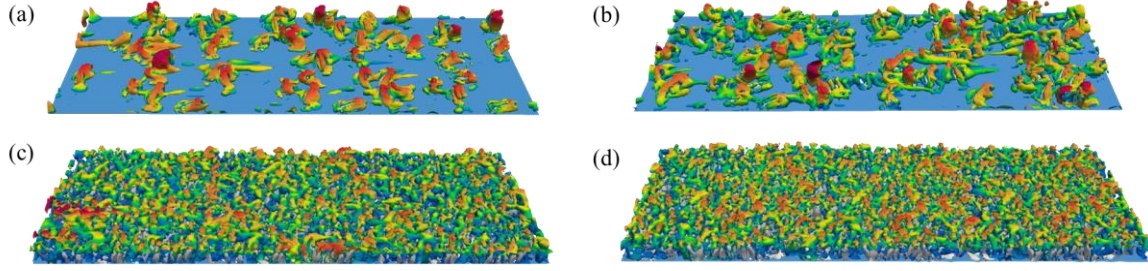


Figure 10. The surface vortex structure with attachment model at $\lambda_2 = 1$, the density of LF: (a) 500 ind/m² (b) 1000 ind/m² (c) 10000 ind/m² (d) 15000 ind/m²

4.3 Manning roughness coefficient

After analyzing the changes of the flow field induced by LF attachment, it is necessary to quantify the flow resistance. In the numerical modeling, the sidewall effect was not considered, and it was assumed that the channel width be infinite in a numerical sense. The following equation is derived from manning equation based on the balance between the flow resistance and the driving force of normal flow.

$$n = H^{\frac{1}{6}} \frac{u_\tau}{U_0 \sqrt{g}} \quad (8)$$

where n is the manning roughness coefficient; u_τ is the shear velocity (m/s); H is the water depth (m); U_0 is the incoming flow velocity (m/s).

In this study, H was set to two constant values: 0.5 m and 5.0 m. u_τ was computed by $u_\tau = \sqrt{\tau_w / \rho}$, where τ_w denotes wall shear stress, which can be obtained by $\tau_w = F_d / A$. F_d and A is the total drag force and the area of LF attachment, respectively.

The manning roughness coefficient (n) was calculated based on the numerical results from various LF attachment densities, U_0 , H_0 . According to the simulation results in Figure 11, LF attachment density has a significant impact on n . The presence of LF caused an immediate increase in n , but as the density increased, n gradually decreased. South LF and north LF showed different variance in n . The peak value of n arrived at density of 1000 ind/m² for south LF, whereas for north LF, it reached its maximum at a density of 7500 ind/m². Additionally, a smaller U_0 led to a smaller n value, along with a steeper decline in n . It should be mentioned that for high-flow scenario, n remained around 0.015, which increased more than 90% comparing to

the cases without LF attachment. Furthermore, in scenarios with deeper water, the transition of the flow regime to skimming flow resulted in a smaller variance of n compared to scenarios with shallower water depth.

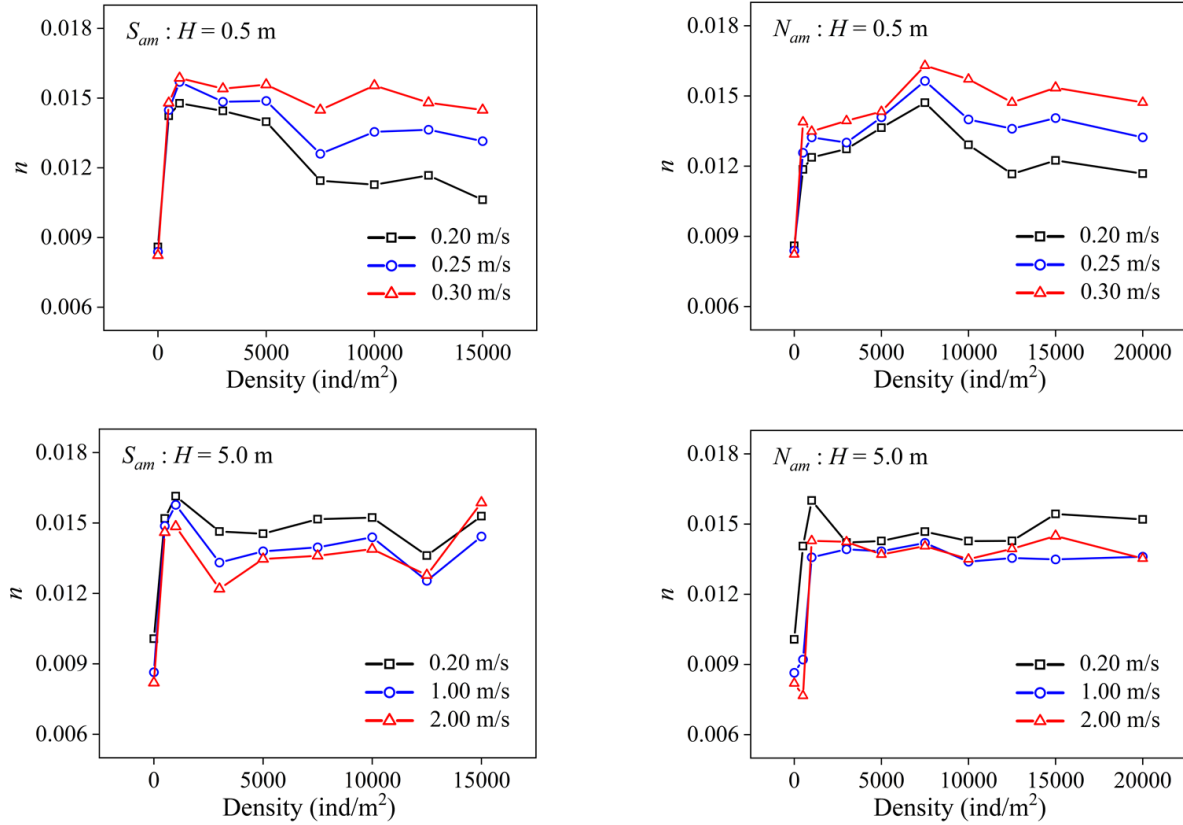


Figure 11. The manning roughness coefficient at different LF attachment densities

Figure 12 shows the n 's variance with roughness concentration (L_c) at different LF attachment densities. Based on the flow regime definition in section 2.5, L_c can be divided into three regimes, as shown in Figure 12. These are the Isolated Roughness Flow (IS), Wake-Interference Flow (WI), and Skimming Flow (SK). In IS regime, n increased rapidly with L_c . As it transitioned to WI regime, n stabilized. Upon reaching skimming flow regime, the overall flow resistance due to LF attachment might decrease with density, wherein the mussel size distribution played a non-negligible role.

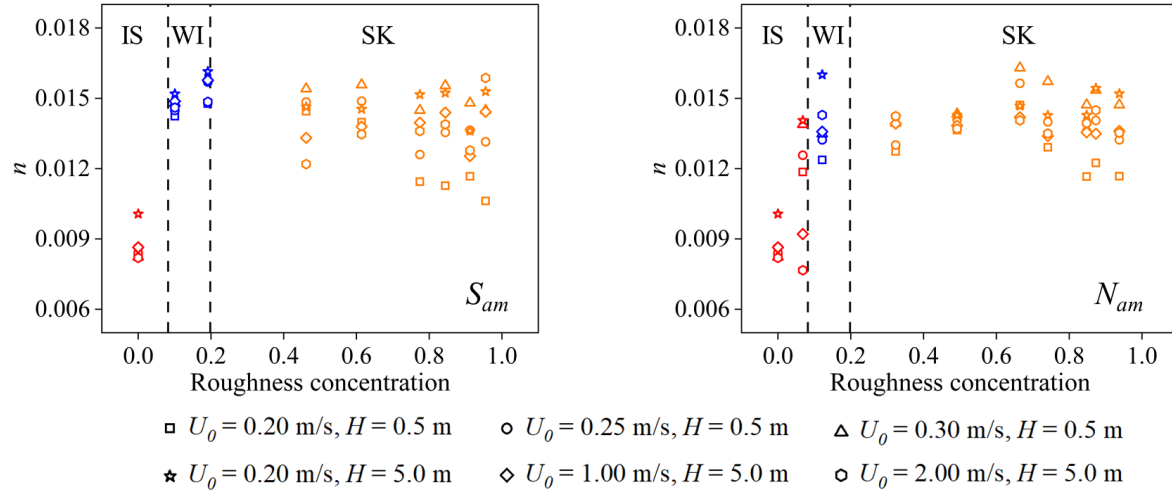


Figure 12. The manning roughness coefficient at different roughness concentrations in the south and north, IS: isolated roughness flow; WI: wake-interference flow; SK: skimming flow

5 Conclusions

The primary focus of this study is to investigate flow structures within *Limnoperna fortunei* attachments and quantitatively assess flow resistance using OpenFOAM. In regard to flow structure, as density gradually increases, the vortex structure on the surface of LF transitions from a clustered formation to a lamellar one. In high-density scenarios, a big wake zone was formed inside LF attachment by the combining effects of individual LF. When quantifying the flow resistance, different densities of attachment produced different flow regimes near the LF: a hydrodynamic phenomenon known as skimming flow occurred when LF densities exceeded 3000 ind/m². The flow regime not only affected the local flow field, but also had a significant impact on the overall flow field. The manning roughness coefficient of the flow field increases with increase attachment density and then gradually stabilizes, and the biggest change rate of manning roughness coefficient is more than 90% compared to the cases without LF attachment. This significantly reduced the water transfer efficiency of the project.

The present physical modeling of attachment only considers a single-layer attachment situation, while in the water transfer project, the attachment density is high enough that the multi-layer attachment phenomenon occurs. Future study will consider the modeling of real attachment and the multi-layer attachment on flow resistance, and further improve the simulation conditions in the consideration of the engineering flow.

Acknowledgments

This work is financially supported by the National Natural Science Foundation of China (52209103) and Open Research Fund Program of State key Laboratory of Hydrosience and Engineering (sklhse-2021-B-03). The data that supports the numerical simulation are obtained from Zhao et al., 2019 and Yang et al., 2024 at <https://doi.org/10.1080/14634988.2019.1698860> and <https://doi.org/10.1016/j.esr.2023.100305>.

Data Availability Statement

Both the geometric models and numerical setups can be obtained by request.

References

- Aberle, J., & Smart, G. M. (2003). The influence of roughness structure on flow resistance on steep slopes. *Journal of Hydraulic Research*, 41(3), 259–269. <https://doi.org/10.1080/00221680309499971>
- Allen, D. C., & Vaughn, C. C. (2010). Complex hydraulic and substrate variables limit freshwater mussel species richness and abundance. *Journal of the North American Benthological Society*, 29(2), 383–394. <https://doi.org/10.1899/09-024.1>
- Barbosa, N. P. U., Ferreira, J. A., Nascimento, C. A. R., Silva, F. A., Carvalho, V. A., Xavier, E. R. S., et al. (2018). Prediction of future risk of invasion by *Limnoperna fortunei* (Dunker, 1857) (Mollusca, Bivalvia, Mytilidae) in Brazil with cellular automata. *Ecological Indicators*, 92, 30–39. <https://doi.org/10.1016/j.ecolind.2018.01.005>
- Boltovskoy, D., Paolucci, E., MacIsaac, H. J., Zhan, A., Xia, Z., & Correa, N. (2022). What we know and don't know about the invasive golden mussel *Limnoperna fortunei*. *Hydrobiologia*. <https://doi.org/10.1007/s10750-022-04988-5>
- Canovaro, F., Paris, E., & Solari, L. (2007). Effects of macro-scale bed roughness geometry on flow resistance. *Water Resources Research*, 43(10), 2006WR005727. <https://doi.org/10.1029/2006WR005727>
- Cataldo, D. H. (2015). Larval Development of *Limnoperna Fortunei*. In D. Boltovskoy (Ed.), *Limnoperna Fortunei* (pp. 43–53). Cham: Springer International Publishing. https://doi.org/10.1007/978-3-319-13494-9_2
- Chen, Y., Liu, X., Gulley, J. D., & Mankoff, K. D. (2018). Subglacial Conduit Roughness: Insights From Computational Fluid Dynamics Models. *Geophysical Research Letters*, 45(20). <https://doi.org/10.1029/2018GL079590>
- Chen, Y., DiBiase, R. A., McCarroll, N., & Liu, X. (2019). Quantifying flow resistance in mountain streams using computational fluid dynamics modeling over structure-from-motion photogrammetry-derived microtopography. *Earth Surface Processes and Landforms*, 44(10), 1973–1987. <https://doi.org/10.1002/esp.4624>

- Constantinescu, G., Miyawaki, S., & Liao, Q. (2013). Flow and Turbulence Structure past a Cluster of Freshwater Mussels. *Journal of Hydraulic Engineering*, 139(4), 347–358. [https://doi.org/10.1061/\(ASCE\)HY.1943-7900.0000692](https://doi.org/10.1061/(ASCE)HY.1943-7900.0000692)
- Davis, J. A., & Barmuta, L. A. (1989). An ecologically useful classification of mean and near-bed flows in streams and rivers. *Freshwater Biology*, 21(2), 271–282. <https://doi.org/10.1111/j.1365-2427.1989.tb01365.x>
- de Medeiros Fortunato, H. F., & Andrade Figueira, R. M. (2022). Freshwater sponges overgrow the invasive golden mussel *Limnoperna fortunei* in the Upper Parana River, Brazil. *Marine and Freshwater Research*, 73(11), 1394–1399. <https://doi.org/10.1071/MF22023>
- Demirel, Y. K., Uzun, D., Zhang, Y., Fang, H.-C., Day, A. H., & Turan, O. (2017). Effect of barnacle fouling on ship resistance and powering. *Biofouling*, 33(10), 819–834. <https://doi.org/10.1080/08927014.2017.1373279>
- de Souza, T. R. C., de Andrade, J. T. M., Serrano, R. O. P., Vidigal, T. H. D. A., Viana, E. M. de F., Bastos, A. S., & Martinez, C. B. (2023). Energy efficiency analysis of pumping systems impacted by the Golden Mussel: A case study in the Brazilian Amazon. *Energies*, 16(4), 1858. <https://doi.org/10.3390/en16041858>
- D'Ippolito, A., Calomino, F., Alfonsi, G., & Lauria, A. (2021). Flow resistance in open channel due to vegetation at reach scale: A Review. *Water*, 13(2), 116. <https://doi.org/10.3390/w13020116>
- Elizarraga, V. H. H., Ballantyne, S., O'Brien, L. G., Americo, J. A., Suhr, S. T., Senut, M.-C., et al. (2023). Toward invasive mussel genetic biocontrol: Approaches, challenges, and perspectives. *Iscience* 26(10), 108027. <https://doi.org/10.1016/j.isci.2023.108027>
- French, S. K., & Ackerman, J. D. (2014). Responses of newly settled juvenile mussels to bed shear stress: implications for dispersal. *Freshwater Science*, 33(1), 46–55. <https://doi.org/10.1086/674983>
- Friedrichs, M., Graf, G., & Springer, B. (2000). Skimming flow induced over a simulated polychaete tube lawn at low population densities. *Marine Ecology Progress Series*, 192, 219–228. <https://doi.org/10.3354/meps192219>
- Ghisalberti, M. (2009). Obstructed shear flows: similarities across systems and scales. *Journal of Fluid Mechanics*, 641, 51–61. <https://doi.org/10.1017/S0022112009992175>
- Fu, X., & Bin, L. (2012). The ecological characteristics research of *Limnoperna fortunei*. *China Rural Water and Hydropower*, (01):18-20+24. (in Chinese)
- Hardison, B. S., & Layzer, J. B. (2001). Relations between complex hydraulics and the localized distribution of mussels in three regulated rivers. *Regulated Rivers: Research & Management*, 17(1), 77–84. [https://doi.org/10.1002/1099-1646\(200101/02\)17:1<77::AID-RRR604>3.0.CO;2-S](https://doi.org/10.1002/1099-1646(200101/02)17:1<77::AID-RRR604>3.0.CO;2-S)
- Haubrock, P. J., Cuthbert, R. N., Ricciardi, A., Diagne, C., & Courchamp, F. (2022). Economic costs of invasive bivalves in freshwater ecosystems. *Diversity and Distributions*, 28(5), 1010–1021. <https://doi.org/10.1111/ddi.13501>
- He, C., Yang, C., & Turowski, J. M. (2021). The effect of roughness spacing and size on the lateral deflection of bedload particles. *Water Resources Research*, 57(10), e2021WR029717. <https://doi.org/10.1029/2021WR029717>
- Ismail, H., Xu, Y., & Liu, X. (2021). Flow and Scour around Idealized Porous Engineered Log Jam Structures. *Journal of Hydraulic Engineering*, 147(1), 04020089. [https://doi.org/10.1061/\(ASCE\)HY.1943-7900.0001833](https://doi.org/10.1061/(ASCE)HY.1943-7900.0001833)

- Jeong, J., & Hussain, F. (1995). On the identification of a vortex. *Journal of Fluid Mechanics*, 285, 69–94.
<https://doi.org/10.1017/S0022112095000462>
- Jing, Z., Chen, H., Cao, H., Tang, X., Shang, Y., Liang, Y., et al. (2022). Spatial and temporal characteristics, influencing factors and prediction models of water quality and algae in early stage of Middle Route of South-North Water Diversion Project. *Environmental Science and Pollution Research*, 29(16), 23520–23544.
<https://doi.org/10.1007/s11356-021-16917-5>
- Khor, Y. S., & Xiao, Q. (2011). CFD simulations of the effects of fouling and antifouling. *Ocean Engineering*, 38(10), 1065–1079. <https://doi.org/10.1016/j.oceaneng.2011.03.004>
- Lazzarin, T., Constantinescu, G., Di Micco, L., Wu, H., Lavignani, F., Lo Brutto, M., et al. (2023). Influence of bed roughness on flow and turbulence structure around a partially-buried, isolated freshwater mussel. *Water Resources Research*, 59(4), e2022WR034151. <https://doi.org/10.1029/2022WR034151>
- Lee, B. E., & Soliman, B. F. (1977). An investigation of the forces on three dimensional bluff bodies in rough wall turbulent boundary layers. *Journal of Fluids Engineering*, 99(3), 503–509. <https://doi.org/10.1115/1.3448828>
- Li, D. (2009). Study on the influence of Golden mussel on the water conveyance capacity of water transfer structures. *Water & Wastewater Engineering*, 45(S1), 94–96. (in Chinese)
<https://doi.org/10.13789/j.cnki.wwel1964.2009.s1.074>
- Liu, W., Xu, M., Zhang, J., & Zhang, T. (2020). Survival and attachment of biofouling freshwater mussel (*Limnoperna fortunei*) to environmental conditions: potential implications in its invasion, infection and biofouling control. *Limnology*, 21(2), 245–255. <https://doi.org/10.1007/s10201-020-00607-1>
- Lopez, J. W., & Vaughn, C. C. (2021). A review and evaluation of the effects of hydrodynamic variables on freshwater mussel communities. *Freshwater Biology*, 66(9), 1665–1679. <https://doi.org/10.1111/fwb.13784>
- Mahapatra, B. B., Das, N. K., Jadhav, A., Roy, A., & Aravind, N. A. (2023). Global freshwater mollusc invasion: pathways, potential distribution, and niche shift. *Hydrobiologia*. <https://doi.org/10.1007/s10750-023-05299-z>
- Manga, M., & Kirchner, J. W. (2000). Stress partitioning in streams by large woody debris. *Water Resources Research*, 36(8), 2373–2379. <https://doi.org/10.1029/2000WR900153>
- Mayaud, J. R., Wiggs, G. F. S., & Bailey, R. M. (2016). Dynamics of skimming flow in the wake of a vegetation patch. *Aeolian Research*, 22, 141–151. <https://doi.org/10.1016/j.aeolia.2016.08.001>
- McEntee, W. (1916). Variation of frictional resistance of ships with condition of wetted surface. *Journal of the American Society for Naval Engineers*, 28(1), 311–314. <https://doi.org/10.1111/j.1559-3584.1916.tb00632.x>
- Menter, F. R. (1994). Two-equation eddy-viscosity turbulence models for engineering applications. *AIAA Journal*, 32(8), 1598–1605. <https://doi.org/10.2514/3.12149>
- Morris, H. M. (1955). Flow in rough conduits. *Transactions of the American Society of Civil Engineers*, 120(1), 373–398.
- Morton, B. (2015). The biology and anatomy of *Limnoperna fortunei*, a significant freshwater bioinvader: blueprints for success. In D. Boltovskoy (Ed.), *Limnoperna Fortunei* (pp. 3–41). Cham: Springer International Publishing.
https://doi.org/10.1007/978-3-319-13494-9_1

- Mossa, M., Ben Meftah, M., De Serio, F., & Nepf, H. M. (2017). How vegetation in flows modifies the turbulent mixing and spreading of jets. *Scientific Reports*, 7(1), 6587. <https://doi.org/10.1038/s41598-017-05881-1>
- Nakano, D., Kobayashi, T., & Sakaguchi, I. (2012). Changes in the drift and the settlement of the freshwater mussel *Limnoperna fortunei* along a headrace channel. *Water Science and Technology*, 65(3), 426–433. <https://doi.org/10.2166/wst.2012.866>
- Nepf, H. M. (2012). Hydrodynamics of vegetated channels. *Journal of Hydraulic Research*, 50(3), 262–279. <https://doi.org/10.1080/00221686.2012.696559>
- Nikora, V. I., Goring, D. G., & Biggs, B. J. F. (1998). On gravel-bed roughness characterization. *Water Resources Research*, 34(3), 517–527. <https://doi.org/10.1029/97WR02886>
- Nugroho, S., Nugroho, B., Fusil, E., & Chin, R. (2023). Effects of varied roughness coverage area on drag in a turbulent boundary layer using numerical simulations. *Ocean Engineering*, 287, 115721. <https://doi.org/10.1016/j.oceaneng.2023.115721>
- Pyšek, P., Hulme, P. E., Simberloff, D., Bacher, S., Blackburn, T. M., Carlton, J. T., et al. (2020). Scientists' warning on invasive alien species. *Biological Reviews*, 95(6), 1511–1534. <https://doi.org/10.1111/brv.12627>
- Ricciardi, A. (1998). Global range expansion of the Asian mussel *Limnoperna fortunei* (Mytilidae): Another fouling threat to freshwater systems. *Biofouling*, 13(2), 97–106. <https://doi.org/10.1080/08927019809378374>
- Sansom, B. J., Bennett, S. J., Atkinson, J. F., & Vaughn, C. C. (2020). Emergent hydrodynamics and skimming flow over mussel covered beds in rivers. *Water Resources Research*, 56(8), e2019WR026252. <https://doi.org/10.1029/2019WR026252>
- Sansom B. J., Atkinson J. F., & Bennett S. J. (2018). Modulation of near-bed hydrodynamics by freshwater mussels in an experimental channel. *Hydrobiologia*, 810(1), 449–463. <https://doi.org/10.1007/s10750-017-3172-9>
- Sansom B. J., Bennett, S. J., & Atkinson, J. F. (2022). Freshwater mussel burrow position and its relation to streambed roughness. *Freshwater Science*, 41(2), 315–326. <https://doi.org/10.1086/719993>
- Schultz, M. P. (2007). Effects of coating roughness and biofouling on ship resistance and powering. *Biofouling*, 23(5), 331–341. <https://doi.org/10.1080/08927010701461974>
- Smith, M. W. (2014). Roughness in the Earth Sciences. *Earth-Science Reviews*, 136, 202–225. <https://doi.org/10.1016/j.earscirev.2014.05.016>
- Song, S., Demirel, Y. K., De Marco Muscat-Fenech, C., Tezdogan, T., & Atlar, M. (2020). Fouling effect on the resistance of different ship types. *Ocean Engineering*, 216, 107736. <https://doi.org/10.1016/j.oceaneng.2020.107736>
- Spalart, P., & Allmaras, S. (1992). A one-equation turbulence model for aerodynamic flows. In *30th Aerospace Sciences Meeting and Exhibit*. Reno, NV, U.S.A.: American Institute of Aeronautics and Astronautics. <https://doi.org/10.2514/6.1992-439>
- Styles, R. (2015). Flow and turbulence over an Oyster Reef. *Journal of Coastal Research*, 314, 978–985. <https://doi.org/10.2112/JCOASTRES-D-14-00115.1>
- Vaughn, C. C., & Hakenkamp, C. C. (2001). The functional role of burrowing bivalves in freshwater ecosystems. *Freshwater Biology*, 46(11), 1431–1446. <https://doi.org/10.1046/j.1365-2427.2001.00771.x>

- Wang, C., Xu, M., Zhang, J., & Zhou, X. (2023). High-latitude invasion and environmental adaptability of the freshwater mussel *Limnoperna fortunei* in Beijing, China. *Ecological Applications*, e2887. <https://doi.org/10.1002/eap.2887>
- Wang, H., Xia, Z., Li, S., MacIsaac, H. J., & Zhan, A. (2023). What's coming eventually comes: a follow-up on an invader's spread by the world's largest water diversion in China. *Biological Invasions*, 25(1), 1–5. <https://doi.org/10.1007/s10530-022-02897-1>
- Wang, P., Wang, C., & Zhu, D. Z. (2010). Hydraulic resistance of submerged vegetation related to effective height. *Journal of Hydrodynamics*, 22(2), 265–273. [https://doi.org/10.1016/S1001-6058\(09\)60054-8](https://doi.org/10.1016/S1001-6058(09)60054-8)
- Wei, X., Liu, D., Zhang, J., Yang, Z., Yang, L., & Wan, X. (2015). The adhesion properties of *Limnoperna fortunei* in water projects. *Journal of China Institute of Water Resources and Hydropower Research*, 13(05):397-400. (in Chinese) <https://doi.org/10.13244/j.cnki.jiwhr.2015.05.014>
- Widdows, J., Lucas, J. S., Brinsley, M. D., Salkeld, P. N., & Staff, F. J. (2002). Investigation of the effects of current velocity on mussel feeding and mussel bed stability using an annular flume. *Helgoland Marine Research*, 56(1), 3–12. <https://doi.org/10.1007/s10152-001-0100-0>
- Widdows, J., Pope, N. D., Brinsley, M. D., Gascoigne, J., & Kaiser, M. J. (2009). Influence of self-organised structures on near-bed hydrodynamics and sediment dynamics within a mussel (*Mytilus edulis*) bed in the Menai Strait. *Journal of Experimental Marine Biology and Ecology*, 379(1–2), 92–100. <https://doi.org/10.1016/j.jembe.2009.08.017>
- Wolfe, S. A., & Nickling, W. G. (1993). The protective role of sparse vegetation in wind erosion. *Progress in Physical Geography: Earth and Environment*, 17(1), 50–68. <https://doi.org/10.1177/030913339301700104>
- Wu, H., & Constantinescu, G. (2022). Effect of angle of attack on flow past a partially-burrowed, isolated freshwater mussel. *Advances in Water Resources*, 168, 104302. <https://doi.org/10.1016/j.advwatres.2022.104302>
- Wu, H., Constantinescu, G., & Zeng, J. (2020). Flow and entrainment mechanisms around a freshwater mussel aligned with the incoming flow. *Water Resources Research*, 56(9), e2020WR027983. <https://doi.org/10.1029/2020WR027983>
- Xu, M., Darrigran, G., Wang, Z., Zhao, N., Lin, C. C., & Pan, B. (2015). Experimental study on control of *Limnoperna fortunei* biofouling in water transfer tunnels. *Journal of Hydro-environment Research*, 9(2), 248–258. <https://doi.org/10.1016/j.jher.2014.06.006>
- Xu, Y., & Liu, X. (2017). Effects of different in-stream structure representations in computational fluid dynamics models—taking engineered log jams (ELJ) as an Example. *Water*, 9(2), 110. <https://doi.org/10.3390/w9020110>
- Xu, Y., & Liu, X. (2021). An immersed boundary method with y^+ -adaptive wall function for smooth wall shear. *International Journal for Numerical Methods in Fluids*, 93(6), 1929–1946. <https://doi.org/10.1002/fld.4960>
- Yan, T., & Sun, Y. (2019). Harm of *Limnoperna fortunei* to pipes of pumps storage power station and corresponding prevention and control. *Mechanical & Electrical Technique of Hydropower Station*, 42(11), 79–81. (in Chinese) <https://doi.org/10.13599/j.cnki.11-5130.2019.11.029>
- Yang, J. Q., & Nepf, H. M. (2019). Impact of vegetation on bed load transport rate and bedform characteristics. *Water Resources Research*, 55(7), 6109–6124. <https://doi.org/10.1029/2018WR024404>

- Yang, Y., Xu, M., Chen, X., Zhang, J., Wang, S., Zhu, J., & Fu, X. (2024). Establishment risk of invasive golden mussel in a water diversion project: An assessment framework. *Environmental Science and Ecotechnology*, 17, 100305. <https://doi.org/10.1016/j.esec.2023.100305>
- Zhan, A., Zhang, L., Xia, Z., Ni, P., Xiong, W., Chen, Y. (2015). Water diversions facilitate spread of non-native species. *Biological Invasions*, 17(11), 3073–3080. <https://doi.org/10.1007/s10530-015-0940-1>
- Zhang, D., Van Der Hoop, J. M., Petrov, V., Rocho-Levine, J., Moore, M. J., & Shorter, K. A. (2020). Simulated and experimental estimates of hydrodynamic drag from bio-logging tags. *Marine Mammal Science*, 36(1), 136–157. <https://doi.org/10.1111/mms.12627>
- Zhang, R., Zhang, Y., Fei, X., Hou, Y., Shi, J., Li, E., & Chu, W. (2022). *Limnoperna fortunei* as an invasive biofouling bivalve species in freshwater: a review of its occurrence, biological traits, risks, and control strategies. *AQUA - Water Infrastructure, Ecosystems and Society*, 71(12), 1364–1383. <https://doi.org/10.2166/aqua.2022.238>
- Zhang, Y., Cheng, J., Hassan, M. A., Wang, P., & Wu, Z. (2024). Drag Coefficient of Emergent Vegetation in a Shallow Nonuniform Flow Over a Mobile Sand Bed. *Water Resources Research*, 60(5), e2023WR036535. <https://doi.org/10.1029/2023WR036535>
- Zhao, N., Xu, M., Blanckaert, K., Qiao, C., Zhou, H., & Niu, X. (2019). Study of factors influencing the invasion of Golden Mussels (*Limnoperna fortunei*) in water transfer projects. *Aquatic Ecosystem Health & Management*, 22(4), 385–395. <https://doi.org/10.1080/14634988.2019.1698860>
- Zimmerman, G. F., & De Szalay, F. A. (2007). Influence of unionid mussels (Mollusca: Unionidae) on sediment stability: an artificial stream study. *Fundamental and Applied Limnology*, 168(4), 299–306. <https://doi.org/10.1127/1863-9135/2007/0168-0299>